ORIGINAL ARTICLE

CrossMark

Modeling and optimization of thermal characteristics for roll grinders

Zhihang Lin[1] · Jianfu Zhang[1,2] · Pingfa Feng[1,2,3] · Dingwen Yu[1] · Zhijun Wu[1]

Abstract

The thermal deformation has a significant effect on the processing precision of the machine tool. In this paper, a simulation model and an experimental method of the thermal performance were proposed for a roll grinder. The calculation methods of thermal boundary conditions including the heat power caused by the spindle motor with water cooling, headstock motor with air cooling and hydrodynamic bearings, the convective heat transfer coefficients of the rotating surface at different spindle speeds, and machine tool contact resistance were provided to establish a high-precision FEM model. Based on the achieved key temperature points in the simulation, thermal characteristic experiments were carried out at different spindle speeds with 18 temperature sensors and three displacement sensors. The experimental results of the temperature field and thermal displacement were then compared with the simulation results to verify the effectiveness of the constructed finite element model. Finally, three kinds of optimization schemes of the roll grinder structure were discussed to further improve the thermal performance. The simulation results indicated that the thermal deformation of the spindle decreased in the X- and Y-axis directions.

1 Introduction

Thermal error in roll grinding is caused by the thermal deformation of the machine structure induced by the change of the temperature field via internal and external heat sources. The thermal error becomes a more significant contribution in the overall error of the machine as the roll grinder accuracy improves [1]. The roll grinder is a specialized machine tool demanding high accuracy for roll grinding, where the roughness of a surface processed by an ordinary roll grinder is 0.2 μm. Therefore, thermal deformation cannot be neglected.

Large numbers of investigations have been carried out on the thermal error of the machine tool, where the studies can be

mainly classified into two categories of machine hardware optimization and thermal error compensation. The optimization of machine hardware has included the use of low-expansion-coefficient materials such as steel-fiber-reinforced concrete as the machine structural components [2]; optimizing the cooling system structure or parameters [3, 4]; using thermal symmetry structures [5] and cell structures [6]; and reducing the contact surface area between the heat sources and the structural parts [7]. However, modification of the machine structure is expensive and time consuming, so studies have tended toward the second category of thermal error compensation. This establishes a relationship between the thermal deformation and the temperatures of the essential points, the spindle speeds, the ambient temperature, and other factors [8]. This has been accomplished through mathematical modeling and by conducting compensation through the built-in compensation function of the computerized numerical control (CNC) system [9], modifying the programmable logic controller program [10], or using external devices to send the pulse signals to the CNC system [11].

The two fundamental problems encountered by thermal error compensation are the optimization of the location and number of the temperature-measurement points, and establishing the thermal error prediction model. Many studies have been reported on the optimization of temperature measurement

✉ Jianfu Zhang
 zhjf@tsinghua.edu.cn

1 Department of Mechanical Engineering, Tsinghua University, Beijing 100084, China

2 State Key Laboratory of Tribology and Beijing Key Lab of Precision/Ultra-precision Manufacturing Equipments and Control, Tsinghua University, Beijing 100084, China

3 Graduate School at Shenzhen, Tsinghua University, Shenzhen 518055, China
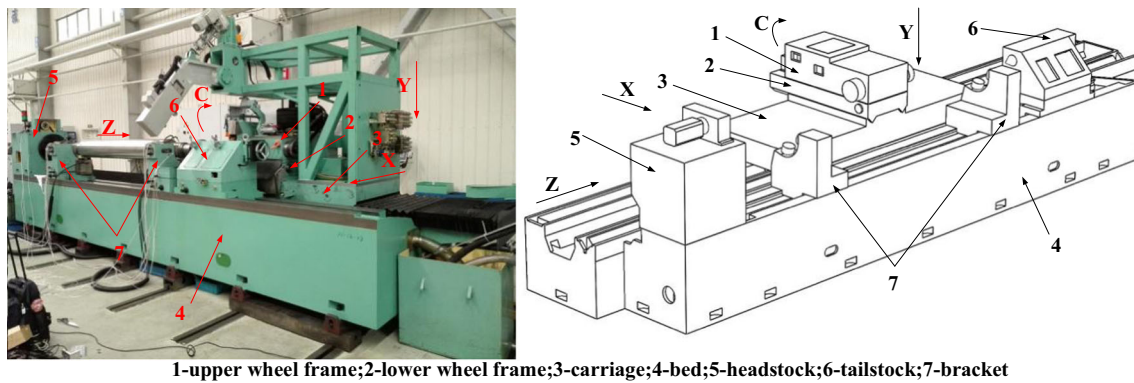
1-upper wheel frame;2-lower wheel frame;3-carriage;4-bed;5-headstock;6-tailstock;7-bracket

Fig. 1 Photograph (left image) and schematic (right image) of a typical roll grinder

points, including fuzzy c-means clustering (FCM) [12], fuzzy clustering [13], correlation analysis [14], and gray relational analysis [15]. Numerous thermal error modeling methods have been proposed, including multiple regression analysis [16], a variety of neural networks [17], adaptive neural fuzzy inferring system [18], state space theory [19], and projection pursuit regression [20]. Various search algorithms have been used in many studies to get the best parameters of the structures [21]. In recent years, more studies have been done using a variety of intelligent algorithms for thermal error modeling, such as ant colony algorithm, artificial fish swarm algorithm [22], particle swarm algorithm [23], cuckoo search algorithm [24], metaheuristic algorithm [25], genetic algorithm [26], and imperialist competitive algorithm [27]. Different optimization algorithms have been compared and investigated [28, 29]. In addition, many hybrid optimization algorithms have been proposed and applied in structural design optimization [30, 31]. All these studies were able to obtain satisfactory compensation results.

The roll grinder, however, is different from a general processing machine tool in three aspects. (1) For higher rotation accuracy and stability, the roll grinder generally uses hydrodynamic bearings to support the spindle owing to the oil film homogenization effect of hydrodynamic bearings. (2) Even when the stroke of the Z-axis of the roll grinder is the greatest, users are more concerned with the movement accuracy of the X-axis rather than that of the Z-axis. (3) In addition to cooling and lubricating, the oil-cooled recirculation system of the roll grinder is used to support the rotation of the spindle. Because of the excessive length of the circulating oil passage length owing to the machine tool structure, the oil temperature fluctuates greatly and causes the machine tool thermal deformation to also fluctuate greatly.

Considering the differences mentioned above, this paper proposes a modeling and experimental method of the thermal characteristics to solve the special requirement of the roll

grinder. First, a thermal-structure coupling finite element model (FEM) is established based on the analysis of the thermal boundary condition, and a series of simulations with different operating condition parameters is carried out to find out the weakness of thermal performance of the entire machine. Second, thermal balance experiments at different spindle speeds are conducted to verify the reliability of FEM simulation by comparing the simulation results with the experiment results. Finally, on the basis of the above, the optimized machine structure is developed, where the simulation results show that the optimized machine structure can decrease the thermal deformation in the X- and Y-axis directions.

2 Modeling and simulation of the roll grinder thermal characteristics

2.1 Structure of a typical roll grinder

As shown in Fig. 1, a typical roll grinder consisted of an upper wheel frame, lower wheel frame, carriage, bed, headstock, tailstock, bracket, and other components. The lower wheel frame moved along the X-axis relative to the carriage, while the carriage moved along the Z-axis relative to the bed. The upper wheel frame rotated around the C-axis relative to the lower wheel frame. The spindle system was equipped with hydrodynamic bearings, where the normal and maximum speeds of the spindle were 700 and 1200 r/min, respectively.

2.2 The roll grinder thermal boundary conditions

2.2.1 Thermal physical parameters of the machine tool material

The materials comprising the main parts of the machine, the hydrodynamic bearings, and the spindle were Q250, ZQSn6-6-3, and 38CrMoAL, respectively. The external environment was the natural convection of air, and the lubricating oil was L-FC15 spindle oil. A wooden board was inserted between the

Table 1 Material thermal properties

	ZQSn6-6-3	38CrMoAL	Q250	Air	L-FC15 spindle oil	Wood board	Water
Elastic modulus (MPa)	1.08×10^5	2.05×10^5	2.02×10^5	–	–	–	–
Poisson ratio	0.35	0.34	0.26	–	–	–	–
Linear expansion coefficient(1/°C)	1.73×10^{-5}	1.23×10^{-5}	1.2×10^{-5}	–	3.48×10^{-4}	–	–
Thermal conductivity (W/m•K)	87.6	37.7	48	2.55×10^{-2}	0.8	0.34	0.58
Specific heat capacity (J/kg•K)	377	435	460	1.0069	1880	2500	4.2×10^3
Density (kg/m³)	8800	7710	7850	1.1769	852	1000	1.0×10^3

spindle motor and the upper wheel frame for isolation purposes, and considering the low thermal conductivity of the board, it was necessary to consider the thermal insulation effects thereof. The thermal properties of the materials used herein according to the material manuals are shown in Table 1.

2.2.2 Heat source analysis

The heat sources of the roll grinder include the heat loss of the spindle motor, the heat loss of the headstock motor, the friction heat of the hydrodynamic bearings, the friction heat between the workpiece and the bracket, the power loss of the pulley, and the grinding heat. The roll grinder machine was idle in the experiment, so the grinding heat was 0.

The spindle motor (Siemens 1PH8135-1DF20-2DA1) had a spindle speed of n and a pulley drive ratio of 1.52, with a resulting spindle motor speed of $1.52n$. According to the speed of the spindle motor, the output power of the spindle motor P_s and the efficiency $h_s = 85\%$ can be obtained in the spindle motor manual. The thermal power of the spindle motor is given as $P_{sh} = P_s(1 - h_s)h_s^{-1}$. The spindle motor is equipped with a water cooling system, and the heat power taken away by cooling water can be calculated by

$$P_{cool} = Q\rho c\Delta t, \tag{1}$$

where P_{cool} is the cooling power; Q is the flow rate of the cooling water; ρ is the density of water; c is the specific heat of water; and Δt is the temperature rise of the cooling water.

The actual heating power of the spindle motor is given as $P_t = P_{sh} - P_{cool}$.

A headstock motor (Siemens 1FK7086-7AF71-1DG2) was used whose rated power was $P_{hN} = 5.7$ kW, efficiency factor was $\eta_{hs} = 93\%$, and which used natural air cooling. The head motor thermal power (P_{hs}) calculation formula is

$$P_{hs} = P_{hN}(1 - \eta_{hs})/\eta_{hs}. \tag{2}$$

A planetary reducer (STOBER PH721F0070ME, Pforzheim, Germany) was used as the headstock reducer whose efficiency was $\eta_g \leq 93$–96% (given by the STOBER company technical manual). The heat of the planetary reducer (P_{gs}) can be calculated as

$$P_{gs} = P_{hN}\left(1 - \eta_g\right), \tag{3}$$

Calculation of the power loss of the headstock synchronous belt (P_{ds}) can be calculated as

$$P_{ds} = P_{hs}\eta g(1 - \eta_d), \tag{4}$$

where η_d is the efficiency of the headstock synchronous belt.

The workpiece was supported by two brackets that each had two bushings, including side and bottom bushings, where the angles between the two bushings and the vertical direction were 90° and 14.91°, respectively. Through geometrical analysis, the ratio of the distance between the two brackets and the centroid of the workpiece was found to be 1.2:1. Also, the total frictional heat between the bushings and the workpiece

Table 2 Heat power transfer via the frictional heat between the bushings and workpiece

Brackets	Bushings	The friction heat power (W)
Left bracket	Side bushing	34
	Bottom bushing	130
Right bracket	Side bushing	28
	Bottom bushing	109

Table 3 Frictional heat power of dynamic bearings at different spindle speeds

Rotating speeds (rpm)	Left bearing (W)	Right bearing (W)
695	625	256
795	775	317
900	939	384
1000	1087	445
1134	1310	536
1200	1349	552

Table 4 Convective heat transfer coefficients of rotating surfaces at different rotation speeds

Rotating speeds (rpm)	Cylindrical surface of spindle motor rotating end (W/m²·°C)	Cylindrical surface of spindle pulley end (W/m²·°C)	Cylindrical surface of spindle wheel end (W/m²·°C)	Round face of spindle motor rotating end (W/m²·°C)	Round face of spindle wheel end (W/m²·°C)	Between the spindle and the spindle oil (W/m²·°C)
695	38.1	34.8	20.8	76.4	68.9	4154.4
795	41.7	38.0	22.8	79.8	71.7	4591.7
900	45.2	41.3	24.8	83.1	74.5	5041.6
1000	48.5	44.3	26.6	86.0	77.0	5462.6
1134	52.8	48.2	28.9	89.8	80.2	6016.9
1200	54.8	50.0	30.0	91.6	81.7	6286.4

equals the mechanical power delivered to the workpiece by the synchronous belt. Considering that 70% of the heat is taken away by the oil gas lubrication and 80% of the remaining heat is transferred into the workpiece, the heat into the four bushings is found to be 302 W. Therefore, using the pressure ratio, the frictional heat powers of the four bushings can be calculated and are given in Table 2.

The heating power of the hydrodynamic bearings can be calculated as [32]

$$P = 1.5\left(\frac{n}{1000}\right)^2 \frac{d^3 l\eta}{h}, \tag{5}$$

where P is the frictional heat power (kW); n is the speed of the spindle (rad/min); d is the diameter of bearings (cm); l is the length of bearings (cm); η is the dynamic viscosity of the oil (kg·s/m²); and h is the thickness of the lubrication layer (μm). The thickness h can be calculated by

$$h = h_0(1 + \varepsilon\cos\theta), \tag{6}$$

where h_0 is the radius gap (70 μm); θ is the bearing circumferential angle; ε is the eccentricity changing with the speed. According to the results of Ma and Taylor [33], the temperature of the side leakage of the bearing is close to the average
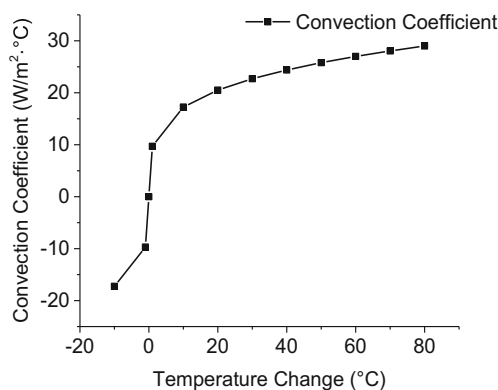
oil temperature of the bearing, and the heat taken away by the lubricating oil accounts for 40 and 60% of the total heat at low speed and high speed, respectively. The frictional heat powers of the left and right bearings at different speeds are shown in Table 3.

2.2.3 The convective heat transfer coefficient

The forced convective heat transfer coefficient between the spindle and the air can be calculated using the Nusselt criterion equation

$$\alpha = \frac{Nu_{air}\cdot\lambda_{air}}{d}, \tag{7}$$

where α is the convective heat transfer coefficient between the rotating surfaces and the fluid, λ_{air} is the thermal conductivity of the fluid, Nu_{air} is the Nusselt number, and d is the equivalent diameter of the rotating body. When the fluid is air, $Re < 4.3 \times 10^5$, and $0.7 < Pr < 670$, the Nusselt number can be calculated by

$$Nu_{air} = 0.133 Re^{2/3} Pr^{1/3}, \tag{8}$$

where Pr is the Prandtl number and Re is the Reynolds number determined by

$$Re = \frac{\omega d_s^2}{\nu_f}, \tag{9}$$

Fig. 2 Natural convection heat transfer coefficient of the high-temperature zone

Table 5 Contact resistance values of the contact surfaces

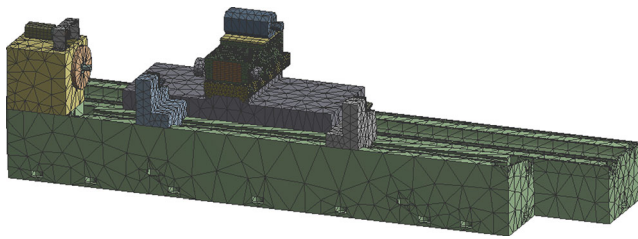| Contact surfaces	Contact resistance (m²·°C/W)
Carriage-bed	1.738×10^{-3}
Wheel frame-carriage	1.738×10^{-3}
Brackets-bed	2.1×10^{-4}
Headstock-bed	8.47×10^{-5}

Fig. 3 FEM mesh model of the roll grinder

where ω is the angular velocity of the spindle, ν_f is the kinematic viscosity of the air, and d_s is the equivalent diameter of the spindle such that

$$d_s = \frac{d_1 l_1 + d_2 l_2 + \cdots d_n l_n}{l}, l = l_1 + l_2 + \cdots l_n, \quad (10)$$

where d_i and l_i are the diameter and the corresponding length of each section of the spindle, respectively. The equivalent diameter of the pulley end (d_1) and the average diameter of the wheel end of spindle (d_2) are 0.18 and 0.115 m, respectively, and the wheel surface equivalent diameter d_3 is 0.5 m. According to the manual, the thermal physical parameters of dry air at 20 °C are $\lambda_{air} = 0.0259$ W/(m·K), $\nu_f = 15.06 \times 10^{-6}$ m²/s, and $Pr_{air} = 0.703$.
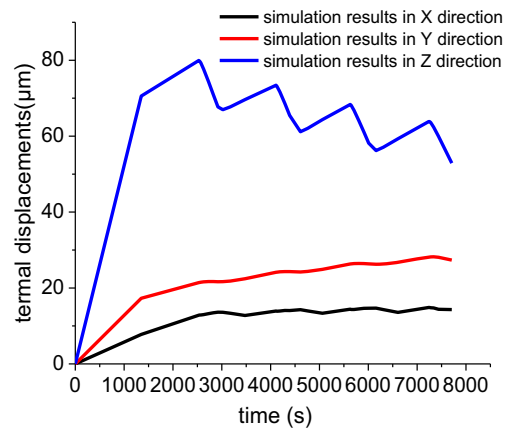

Fig. 5 Simulated curves of the thermal displacement in the three directions with the spindle speed of 1200 rpm

When the fluid is spindle oil, whose physical property parameters are shown in Table 1, the thermal physical parameters are a thermal conductivity of $\lambda_{oil} = 0.8$ W/(m·K) and a kinematic viscosity of $\nu_{oil} = 15.16 \times 10^{-6}$ m²/s. Further, $Pr_{air} = c_p \rho_{oil} \nu_{oil} / \lambda_{oil} = 30.35$, where the specific heat is $c_p = 1880$ J/(kg·K) and the density is $\rho_{oil} = 852$ kg/m³.

Temperature Field

X-axis thermal deformation

Y-axis thermal deformation
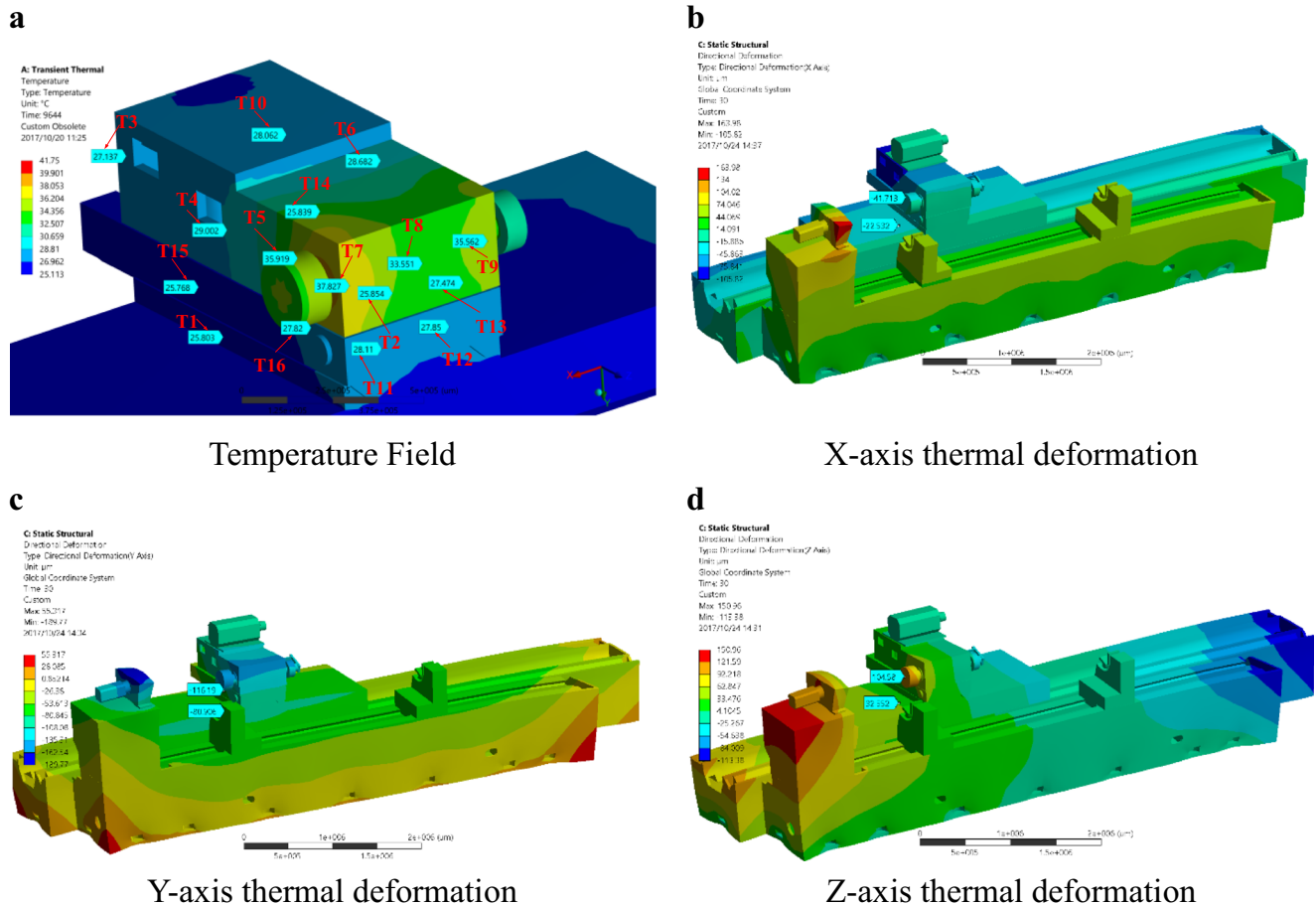

Z-axis thermal deformation

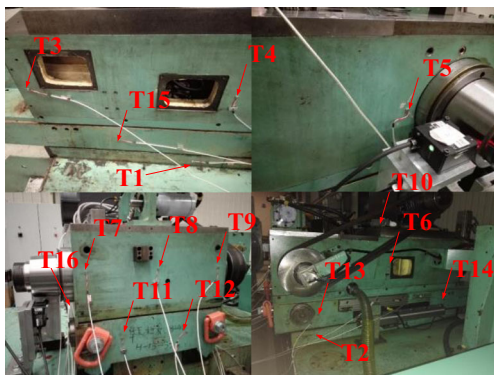Fig. 4 Simulation results of the temperature and thermal displacement with 1200 rpm rotating speeds

Fig. 6 Temperature sensor locations

By analyzing the data above and the size of the rotating body of the machine tool, the convective heat transfer coefficients of the rotating surface at different spindle speeds can be obtained and are shown in Table 4.

Among the temperatures to be measured, that of the oil between the spindle and hydrodynamic bearings is difficult to measure, and was therefore inferred from the temperature of the oil in the oil tank. The temperature of the oil in the oil tank fluctuated between 34 and 37.7 °C, and the temperature of the oil in the cave of the upper wheel frame fluctuated between 39.1 and 41.3 °C. The oil cooler was initiated when the temperature of the oil in the oil tank was detected to be higher than 35 °C, so the oil into the bearing fluctuated between 25 and 34 °C, and the temperature of the oil between the spindle and hydrodynamic bearings fluctuated between 33.4 and 35 °C.

The spindle oil flowed out through the hydrodynamic bearing to form a layer in the cavity of the upper wheel frame. Because the velocity of the flow was very low, the heat exchange between the oil and the upper wheel frame corresponded to natural convection heat transfer, whose coefficient is 41.48 W/(m²•°C) according to the formula of the natural convection heat transfer coefficient [34].

For the other static surfaces that exchanged heat with the air, according to engineering experience, most areas where the temperature is not excessively high have a heat transfer

Fig. 7 Displacement sensors used to measure thermal displacements

coefficient of $\alpha_s = 9.7$ W/(m²•°C). However, when the temperature difference between the wall and the fluid is large, it is not suitable to use a constant composite heat transfer coefficient, according to the heat transfer convection formula. Thus, for the higher-temperature surfaces (i.e., the head motor and grinding wheel motor surfaces) the convective heat transfer coefficient varied according to the temperature difference between the ambient temperature and the wall. The natural convection heat transfer coefficients of the high-temperature zone with various temperature differences were calculated and are shown in Fig. 2.

2.2.4 The machine tool contact resistance

According to the study in [35], the thermal contact resistance has a great influence on the FEM simulation results, and many of the factors that affect the contact resistance are non-linear. The experimental formula for the thermal resistance is given in the form of positive pressure, and the other factors are expressed as fixed coefficients under certain contact conditions, such that [36].

$$R_c = a + b/P_n, \tag{11}$$

where R_c is the unit-area contact thermal resistance; P_n is the unit-area pressure of the contact surface; and a and b are fixed coefficients determined by the experiment.

We have obtained data from a large number of experiments of the thermal properties of the contact surface. Substituting these experimental data into Eq. (11) and fitting the data by the least squares method, the thermal resistance database of the joint surface was constructed.

Using the material properties and surface morphology of the components on both sides of the joint surface, the contact medium and the pressure, and substituting these parameters into the thermal resistance database of the joint surface, we could obtain the thermal resistance at the critical joint surface. This is shown in Table 5.

2.3 Thermal performance FEM simulation

To determine the thermal performance of the roll grinder, a FEM simulation was obtained in the ANSYS workbench by importing the geometric model established in the SOLIDWORKS as shown in Fig. 3. For the regular parts, a hexahedral mesh was generated; and for the irregular parts, a tetrahedral mesh was generated. The FEM comprised 517,232 nodes and 179,632 units.

Substituting the thermal boundary condition parameters obtained in Section 2.2 into the ANSYS workbench, the transient temperature field was obtained via transient thermal analysis. Taking the spindle speed of
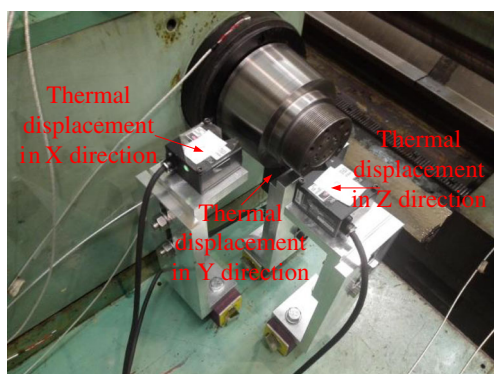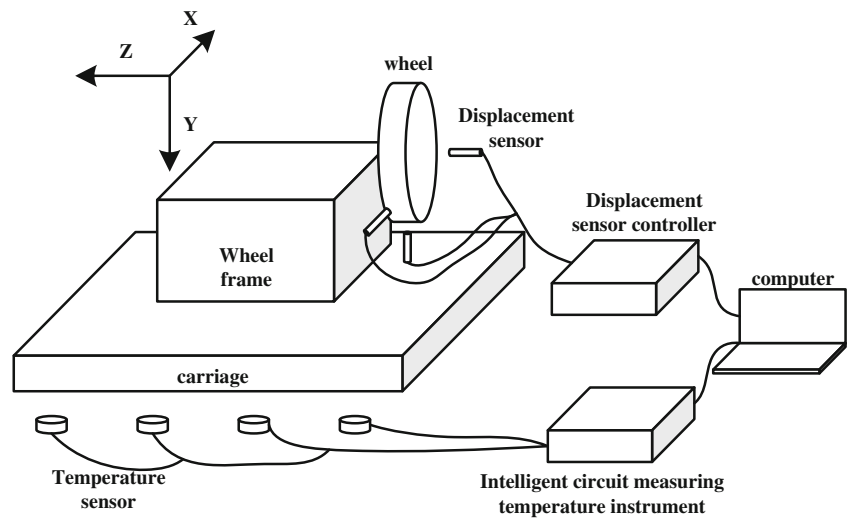
Fig. 8 Schematic diagram of experimental measurement setup

1200 rpm as an example and taking the temperature field obtained above as the load, the displacement field was obtained through structural analysis, as shown in Fig. 4. Further, the simulation curve of the thermal displacements could be obtained, as shown in Fig. 5.

According to the temperature field shown in Fig. 4a, 16 spots were marked as the key temperature points, which were used to determine the locations of the temperature sensors for experimental investigations, by the following principles: (1) Because the left and right hydrodynamic bearings of the spindle system have different sizes, the friction heat powers of the left and right hydrodynamic bearings are different. This creates an asymmetric temperature field, for which the temperature points were marked on both sides. (2) The heat sources are mainly concentrated in the upper wheel frame, and the locations of the upper wheel frame near the heat sources are needed to select as the measuring points. (3) The temperature measuring points are more intensive in the components closer to the heat sources. Thus, the number of temperature measuring points decreases in

the order of the upper wheel frame, the lower wheel frame, and the carriage. (4) The temperature measurement points herein are not used for the thermal error compensation, but for a more accurate and comprehensive understanding of the temperature field distribution of the machine. (5) In addition to the temperature of key components of the machine, the ambient temperature and oil temperature are also necessary.

3 Experiments on the thermal characteristics of the roll grinder

3.1 Experimental setup

Referring to the marked key temperature points in the simulation, the frictional heat between the hydrodynamic bearings and the spindle is the main heat source, while the main thermal deformation areas are the upper and lower
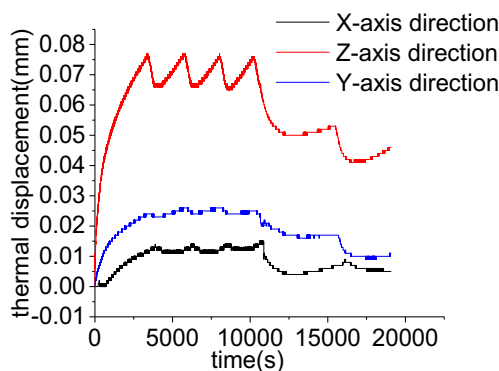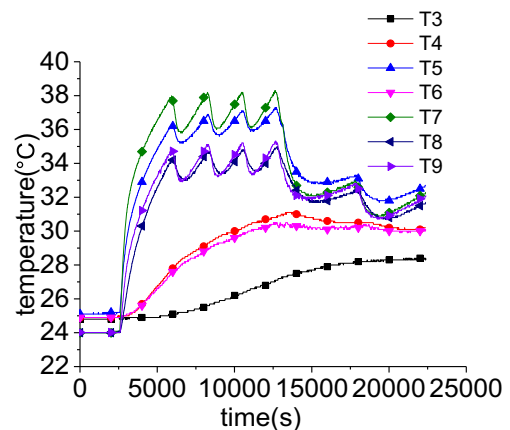

Fig. 9 Thermal displacement of the spindle
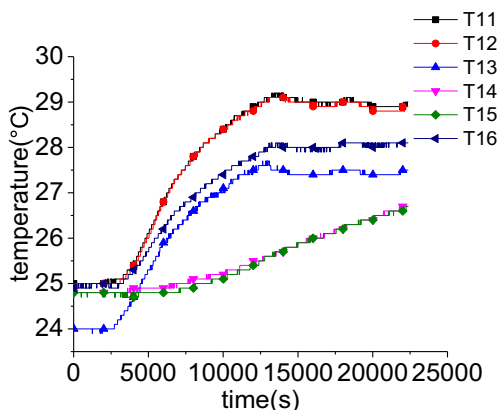

Fig. 10 Temperature of the upper wheel frame

Fig. 11 Temperature of the lower wheel frame

Table 7 Average thermal equilibrium displacements of simulation and experimental results

Axis	Experimental value (μm)	Simulation value (μm)	Absolute error (μm)	Relative error (%)
X	12.3	13.95	1.65	13.4
Y	24.4	24.77	0.37	1.5
Z	70.1	66.64	3.46	− 4.9

wheel frames. Therefore, 14 temperature sensors were located on the surfaces of the upper and lower wheel frames. The temperature of the lubricating oil between the bearings and the spindle was difficult to measure, and thus the temperature of the tank oil was measured instead. Two temperature sensors were used to measure the temperature of the carriage and one sensor for the ambient temperature. Eighteen STT-F-type PT100 temperature sensors (Sailing Technology Corp, Beijing, China) in total were used to measure the temperature change during the experiments, as shown in Fig. 6. The temperature data was transmitted to a computer through a temperature inspection device with a measurement interval of 10 s.

Three LK-H020-type charge-coupled device laser displacement sensors (KEYENCE Corp, Osaka, Japan) were used to measure the X-, Y-, and Z-direction thermal distortions of the machine tool spindle, with a measurement interval of 1 s. The thermal displacement measurement setup is shown in Fig. 7.

3.2 Experimental measuring scheme

Before installing the sensors, the machine was placed in a downtime for one night to ensure that it was in a completely cooled state. The experimental measurement setup is shown in Fig. 8.

Because the heat powers of sources of the machine are different at different speeds, the experiments were carried out at six different speeds to study the temperature field and thermal deformation of the machine under different spindle speeds. During the experiment, the positions of the feed axes of the machine and the spindle speed were constant. When the temperature field curve tends to be constant, the machine can be regarded as in thermal equilibrium. At this point, the machine was stopped, cooled, and measured for some time.

3.3 Experimental measurement results

Taking the spindle speed of 1200 rpm as an example, the thermal displacements as a function of time in the X-, Y-, and Z-axis directions are shown in Fig. 9, and the temperature curves of the sensors on the upper and lower wheel frames as a function of time are shown in Figs. 10 and 11, respectively. The thermal deformation in the Z-axis is the greatest but

Table 6 Comparison of the highest temperature of the simulation and experimental results

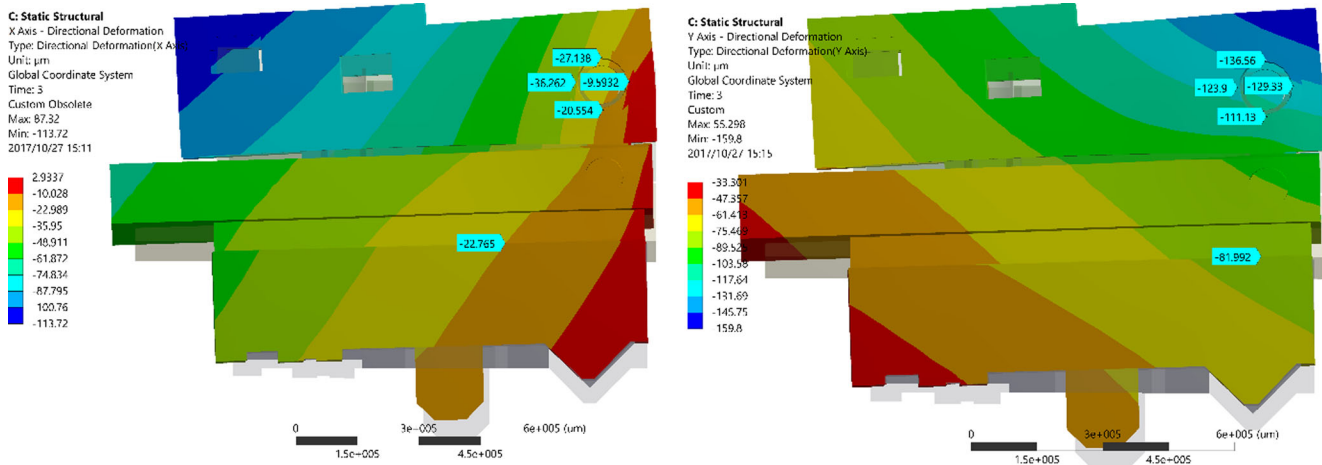| The location of temperature sensors	Experimental value (°C)	Simulation value (°C)	Simulation error (%)
The middle of the left surface of the upper wheel frame (T2)	31.1	30.46	−2.1
The right of the left surface of the upper wheel frame (T5)	37.3	34.92	−6.4
The left of the front surface of the upper wheel frame (T7)	38.3	37.80	−1.3
The right of the front surface of the upper wheel frame (T9)	35.3	35.78	1.4
The middle of the front surface of the upper wheel frame (T8)	35.0	33.55	−4.1
The left surface of the lower wheel frame (T16)	28.1	28.50	1.4
The right surface of the lower wheel frame (T13)	29.2	29.20	0.0
Carriage (T1)	26.9	27.13	0.9

Fig. 12 Contours of the thermal deformation in the X-direction (left) and Y-direction (right)

this direction has little effect on the processing quality of the roll grinder, so the X- and Y-axes were selected as the research targets.

3.4 Comparison of simulation and experimental results

In the transient thermal analysis, we selected the positions of the seven temperature sensors on the FEM, and the temperature field curves of these seven positions were obtained by post-processing. The simulation and experimental results for the highest temperatures at these seven points are shown in Table 6. And, the comparison between the average thermal equilibrium displacements of the simulation results and the experimental results is shown in Table 7. Simulation errors of the temperature and displacement showed that the proposed simulation model has relatively high simulation accuracy.

4 Optimization of roll grinder structure

According to the simulation and experimental analysis, it can be seen that the upper wheel frame has the greatest influence on the thermal displacement. Therefore, based on the thermal

performance simulation method of the roll grinder proposed above, three optimization schemes of the upper wheel frame were discussed mainly aiming to reduce the thermal displacements of the X- and Y-direction: (1) changing the position of the mounting hole where the spindle is placed to be located at the zero-thermal-deformation position of the upper wheel frame; (2) increasing the heat dissipation area of the high-temperature area; (3) adding a structure in the upper wheel frame to absorb thermal distortion.

4.1 Changing the spindle position

As shown in Fig. 12, the spindle mounting hole is located on the upper wheel frame. According to the FEM analysis, the zero-thermal-deformation position where the upper wheel frame is relative to the fixed point of the magnetic seat on the carriage is located on the right and lower sides of the spindle mounting hole, as shown in Fig. 13. By changing the horizontal and vertical positions of the spindle mounting hole, the relationship between the X-direction thermal deformation and the position of the spindle mounting hole is obtained by simulation. (1) The horizontal position has a greater effect on the thermal deformation in the X-direction than the
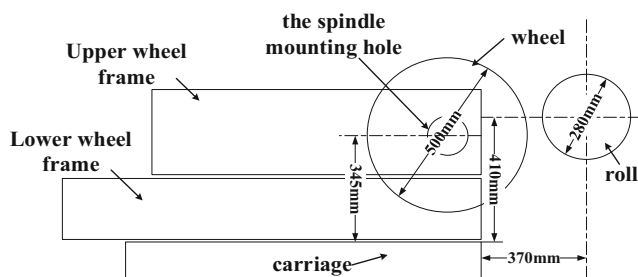

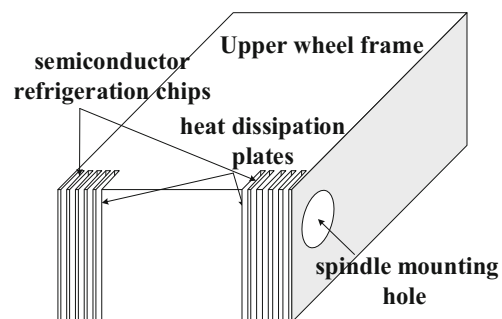**Fig. 13** Position of the spindle mounting hole

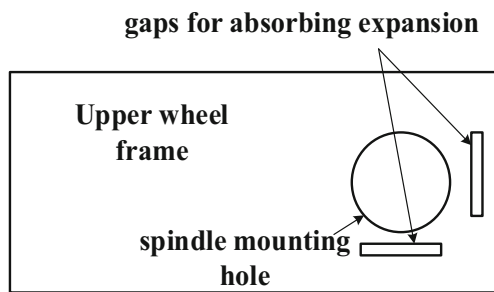**Fig. 14** Location of the heat dissipation plates

Fig. 15 Location of gaps for absorbing expansion

vertical position. (2) The X- and Y-direction thermal deformations are reduced with the change of position of the spindle mounting hole to the right and down.

4.2 Adding heat dissipation plates

According to the previous analysis, the main heat source that causes thermal deformation of the upper wheel frame is the dynamic pressure bearing; therefore, heat dissipation plates are added on the upper wheel frame near the dynamic bearings, as shown in Fig. 14.

The scheme not only increases the heat dissipation area in the high-temperature region, thereby reducing the temperature rise, but also changes the relative position between the spindle mounting hole and the upper wheel frame. The relationship between the thermal deformation in the X-axis direction and the size and location of the heat dissipation plate is obtained by simulation: (1) The width, thickness, and height of the heat dissipation plate have a greater influence on the thermal deformation in the X-axis direction of the machining precision

Table 8 Optimum size for each scheme

Scheme	The best sizes
Schemes 1	The position of the spindle mounting hole is moved 50 mm right and down
Schemes 2	Adding ten heat dissipation plates with 5 mm width, 5 mm interval, 275 mm length, and 50 mm thickness on each side of the upper wheel frame
Schemes3	Adding gaps for absorbing expansion with 5 mm width and 150 mm length on both sides

than the other parameters. (2) With increasing width, thickness, and height of the heat dissipation plates, thermal deformation in the X-axis direction is reduced.

4.3 Adding gaps to absorb expansion

As shown in Fig. 15, gaps for absorbing expansion are symmetrically distributed on both sides of the upper wheel frame. These gaps can absorb some of the thermal deformation, thereby reducing the thermal distortion in the X- and Y-axis directions.

The relationship between the thermal deformation in the X- and Y-axis directions and the size and location of the gaps is obtained by simulation: (1) The depth, horizontal position, and length of the gaps have a greater influence on the thermal deformation in the X-axis direction. (2) Increasing the depth, horizontal position, and length of the gaps reduces the thermal deformation in the X- and Y-axis directions. It is also found, however, that the gaps can lead to a reduction of the static stiffness of the spindle in the X- and Y-axis directions, so it is necessary to balance the thermal deformation and the static stiffness.

4.4 Comparison of before and after optimization

The allowable range of the positions and sizes can be obtained by analyzing the interference condition of each of the above schemes. Then, the optimal sizes of each optimization scheme can be determined according to the relationship between the size and location parameters and the thermal deformation in the X-direction above, as shown in Table 8.

By replacing the upper wheel frame in the roll grinder assembly and considering the effect of the new structural changing, a comparison of the thermal displacement between the non-optimized and optimized structures was conducted based on the proposed simulation method, and the results are shown in Table 9. It indicated that all these modifications could better decrease the thermal deformation in the X- and Y-axis directions. The thermal displacement in the Z-direction became larger. The main reason was that we did not consider its influence because the requirement of position errors along the Z-direction was very low in this case. Moreover, the

Table 9 Reduction of the thermal displacement after optimization

	The thermal displacement (μm)			Relative reduction (%)		
	X-direction	Y-direction	Z-direction	X-direction	Y-direction	Z-direction
Scheme 1	10.31	21.88	86.77	−26	−12	30
Scheme 2	7.70	18.83	93.09	−45	−24	40
Scheme 3	12.99	19.15	86.29	−7	−23	29
Integrated schemes (combining 1~3 schemes)	10.83	21.52	87.27	−22	−13	31

simulation results of integrated schemes indicated that it could not improve the thermal performance.

5 Conclusion

To improve the thermal characteristics of a roll grinder, which is different from a general processing machine tool in many aspects, the following conclusions were obtained by FEM simulation analysis and thermal equilibrium measurement experiment:

(1) An FEM simulation model of the thermal performance was established for a roll grinder by analyzing the thermal boundary conditions. The proposed simulation method considered the changing natural convection heat transfer coefficient of a high-temperature zone with a varying temperature as well as the cooling oil temperature fluctuation of the roll grinder, which caused the simulation to more closely reflect the actual situation.

(2) Thermal characteristic experiments on the temperature field and thermal displacement were carried out at different spindle speeds. The comparison between the average thermal equilibrium displacements of the simulation results and the experimental results was then done. Simulation errors of the temperature and displacement showed that the proposed simulation model has relatively high simulation accuracy.

(3) To further improve the thermal performance of the roll grinder, three types of thermal structure optimization schemes were proposed. The simulation results confirmed that the thermal deformation of the roll grinder was reduced with these schemes. An optimized structure combining these three schemes could not further reduce the thermal displacement, signifying that the thermal structure optimization is not linearly superimposed.

Publisher's Note Springer Nature remains neutral with regard to jurisdictional claims in published maps and institutional affiliations.

References

1. Ramesh R, Mannan MA, Poo AN (2000) Error compensation in machine tools—a review. Part II: thermal errors Int J Mach Tool Manuf 40(9):1257–1284. https://doi.org/10.1016/S0890-6955(00)00010-9

2. Rahman M, Mansur MA, Feng Z (1995) Design, fabrication and evaluation of a steel fibre reinforced concrete column for grinding machines. MATER DESIGN 16(4):205–209. https://doi.org/10.1016/0261-3069(95)00038-0

3. Zhang JF, Feng PF, Chen C, Yu DW, Wu ZJ (2013) A method for thermal performance modeling and simulation of machine tools. Int J Adv Manuf Technol 68(5–8):1517–1527. https://doi.org/10.1007/s00170-013-4939-4

4. Bucuresteanu A, Prodan D, Balan E, Motomancea A (2016) Modernization of cooling units for tools and workpieces in machine tools. Proc Manuf Syst 11(1), 41):41–46

5. Zhang JF, Feng PF, Wu ZJ, Yu DW, Chen C (2013) Thermal structure design and analysis of a machine tool headstock. Mechanika 19(4):478–485. https://doi.org/10.5755/j01.mech.19.4.5044

6. He Y, Fu JZ, Chen ZC (2010) Research on the thermal property of machine tool slides based on cellular structures. Key Eng Mater 426-427:422–426. https://doi.org/10.4028/www.scientific.net/KEM.426-427.422

7. Jiao Y, Sun LJ, Hong HB, Yin YH (2015) Material thermal conductivity determination and structure optimization of ultraprecision optical machine tool. J Mech Eng 51(1):167–175. https://doi.org/10.3901/JME.2015.01.167

8. Ramesh R, Mannan MA, Poo AN (2003) Thermal error measurement and modelling in machine tools. Part I Influence of varying operating conditions. Int J Mach Tool Manuf 43(4):391–404. https://doi.org/10.1016/S0890-6955(02)00263-8

9. Cui LY, Gao WG, Zhang DW, Zhang HJ, Han L (2011) Thermal error compensation for telescopic spindle of CNC machine tool based on SIEMENS 840D system. Trans Tianjin Univ 17(5):340–343. https://doi.org/10.1007/s12209-011-1619-z

10. Pahk HJ, Lee SW (2002) Thermal error measurement and real time compensation system for CNC machine tools incorporating the spindle thermal error and the feed axis thermal error. Int J Adv Manuf Technol 20:487–494. https://doi.org/10.1007/s001700200182

11. Luo W (2010) Thermal error measurement and compensation of CNC machine tools. the Degree of Master of Engineering in Nanjing University of Aeronautics and Astronautics

12. Wang LP, Wang HT, Li TM, Li FC (2015) A hybrid thermal error modeling method of heavy machine tools in z-axis. Int J Adv Manuf Technol 80(1–4):389–400. https://doi.org/10.1007/s00170-015-6988-3

13. Zhang T, Ye WH, Liang RJ, Lou PH, Yang XL (2013) Temperature variable optimization for precision machine tool thermal error compensation on optimal threshold. Chin J Mech Eng-En 26(1):158–165. https://doi.org/10.3901/CJME.2013.01.158

14. Yang J, Shi H, Feng B, Zhao L, Ma C, Mei XS (2015) Thermal error modeling and compensation for a high-speed motorized spindle. Int J Adv Manuf Tech 77(5–8):1005–1017. https://doi.org/10.1007/s00170-014-6535-7

15. Yan J, Yang J (2009) Application of synthetic grey correlation theory on thermal point optimization for machine tool thermal error compensation. Int J Adv Manuf Technol 43(11):1124–1132. https://doi.org/10.1007/s00170-008-1791-z

16. Ruijun L, Wenhua Y, Zhang HH, Qifan Y (2012) The thermal error optimization models for CNC machine tools. Int J Adv Manuf Technol 63(9–12):1167–1176. https://doi.org/10.1007/s00170-012-3978-6

17. Yang H, Ni J (2005) Dynamic neural network modeling for nonlinear, nonstationary machine tool thermally induced error. Int J Mach Tools Manuf 45:455–465. https://doi.org/10.1016/j.ijmachtools.2004.09.004

18. Abdulshahed AM, Longstaff AP, Fletcher S, Myers A (2015) Thermal error modelling of machine tools based on ANFIS with fuzzy c-means clustering using a thermal imaging camera. Appl Math Model 39:1837–1852. https://doi.org/10.1016/j.apm.2014.10.016

19. Gomez-Acedo E, Olarra A, Orive J, LopezdelaCalle L (2013) Methodology for the design of a thermal distortion compensation for large machine tools based in state-space representation with Kalman filter. Int J Mach Tools Manuf 75:100–108. https://doi.org/10.1016/j.ijmachtools.2013.09.005

20. Qianjian G, Jianguo Y (2011) Application of projection pursuit regression to thermal error modeling of a CNC machine tool. Int J Adv Manuf Technol 55(5–8):623–629. https://doi.org/10.1007/s00170-010-3114-4

21. Yildiz BS, Lekesiz H, Yildiz AR (2016) Structural design of vehicle components using gravitational search and charged system search algorithms. Materialprufung 58(1):79–81

22. Guo QJ, Xu RF, Yang TY, He L, Cheng X, Li ZY, Yang JG (2015) Application of GRAM and AFSACA-BPN to thermal error optimization modeling of CNC machine tools. Int J Adv Manuf Technol 83:995–1002. https://doi.org/10.1007/s00170-015-7660-7

23. Yildiz AR, Solanki KN (2012) Multi-objective optimization of vehicle crashworthiness using a new particle swarm based approach. Int J Adv Manuf Technol 59(1–4):367–376

24. Yildiz AR (2013) Cuckoo search algorithm for the selection of optimal machining parameters in milling operations. Int J Adv Manuf Technol 64(1–4):55–61

25. Kiani M, Yildiz AR (2016) A comparative study of non-traditional methods for vehicle crashworthiness and nvh optimization. Arch Comput Method E 23(4):723–734

26. Yildiz BS (2017) A comparative investigation of eight recent population-based optimisation algorithms for mechanical and structural design problems. Int J Vehicle Des 73(1/2/3):208

27. Yildiz BS, Yildiz AR (2017) Moth-flame optimization algorithm to determine optimal machining parameters in manufacturing processes. Materialprufung 59(5):425–429

28. Yildiz AR (2013) Comparison of evolutionary-based optimization algorithms for structural design optimization. Eng Appl Artif Intell 26(1):327–333

29. Yildiz BS, Yildiz AR (2018) Comparison of grey wolf, whale, water cycle, ant lion and sine-cosine algorithms for the optimization of a vehicle engine connecting rod. Mater Test 60(3):311–315

30. Lekesiz H, Yildiz BS (2017) Fatigue-based structural optimisation of vehicle components. Int J Vehicle Des 73(1/2/3):54

31. Yildiz AR, Pholdee N, Bureerat S (2017) Hybrid real-code population-based incremental learning and differential evolution for many-objective optimisation of an automotive floor-frame. Int J Vehicle Des 73(1/2/3):20

32. Von Dobbeler C, Moeller F, Werr T (1953) Leitfaden der Elektrotechnik: Konstruktion elektrischer Maschinen. Teubner

33. Ma MT, Taylor CM (1996) An experimental investigation of thermal effects in circular and elliptical plain journal bearings. Tribol Int 29(1):19–26

34. Uhlmann E, Hu JM (2012) Thermal modelling of an HSC machining centre to predict thermal error of the feed system. Prod Eng 6(6):603–610. https://doi.org/10.1007/s11740-012-0406-6

35. Yang ZW, Yin GF, Xin S, Hua J, Zhong KY (2011) Coupling analysis model of thermal and dynamic characteristics for high-speed motorized spindle. J Jilin Univ 41(1):100–105

36. Li DX, Feng PF, Zhang JF, Wu ZJ, Yu DW (2014) Calculation method of convective heat transfer coefficients for thermal simulation of a spindle system based on RBF neural network. Int J Adv Manuf Technol 70(5–8):1445–1454. https://doi.org/10.1007/s00170-013-5386-y